JOURNAL OF CHEMICAL PHYSICS VOLUME 114, NUMBER 4 22 JANUARY 2001

Chemoconvection: A chemically driven hydrodynamic instability

M. A. Bees[a)]
Department of Mathematics and Statistics, University of Surrey, Guildford, GU2 7XH, United Kingdom

A. J. Pons
Departament de Química Física, Universitat de Barcelona, 08028 Barcelona, Spain and Department of Chemistry, H. C. Ørsted Institute, University of Copenhagen, DK-2100 Copenhagen, Denmark

P. G. Sørensen
Department of Chemistry, H. C. Ørsted Institute, University of Copenhagen, DK-2100 Copenhagen, Denmark

F. Sagués
Departament de Química Física, Universitat de Barcelona, 08028 Barcelona, Spain

(Received 3 July 2000; accepted 27 October 2000)

We describe theory and experiments concerning a chemical reaction, the alkaline oxidation of glucose with methylene blue as a catalyst, that is hypothesized to drive fluid motion via an overturning instability, as an example of a ''chemoconvective'' process. A theoretical model is developed to explain this phenomenon and linear analyses from steady and pseudosteady states are used to predict the basic length and time scales of the patterns which initially appear. These theoretical predictions, using kinetic parameters from recent independent experiments, are contrasted with results from pattern initiation experiments. Preliminary comparisons indicate good qualitative and quantitative agreement. © *2001 American Institute of Physics.*

[DOI: 10.1063/1.1333757]

I. INTRODUCTION

The phenomenon of Rayleigh–Bénard convection has been investigated for many years (e.g., Chandrasekar).[1] It arises when a destabilizing negative vertical temperature gradient is applied across a horizontal layer of fluid and results in either regular or turbulent fluid flows. More recently, bioconvection has been studied in great detail as a similar, but biological, system in which the main difference is that the energy is input into the fluid flow by the biased random swimming motions of individual microorganisms. In particular, in the absence of secondary factors, the microorganisms may swim upwards, on average, in response to gravity,[2,3] light,[4] or a chemical gradient (e.g., oxygen),[5] whereby their excess material density can drive an overturning instability. Additionally, mean balances between fluid torques, and other external torques, acting on the autonomous cells can result in a whole range of aggregative mechanisms and hydrodynamic instabilities.[6–8] We show that there is an analogous chemical system for which the energy for the instability is derived from a chemical reaction modifying the fluid composition, in such a way that the instability can be explained purely from fundamental physicochemical properties. Oxygen diffuses into the fluid at the upper boundary and quickly oxidizes a key clear chemical component, which turns blue. This blue component slowly interacts with glucose in the system, producing the original clear component and a denser reaction product. This product accumulates at the upper surface and can cause an overturning instability made apparent by the appearance of blue dots or lines in the regions where the fluid is down-welling. We describe succinctly this overturning instability due to chemical reaction (and perhaps other chemically driven hydrodynamic instabilities) and the resulting patterns by the term ''chemoconvection.'' We address both experimental and theoretical approaches in this article, but make frequent references to the predominantly experimental report by Pons *et al.*,[9] hereafter referred to as PSBS, in which the kinetics and pattern development of the system are explored in greater detail. In a work in progress we shall systematically study the experimentally observed wavelengths associated with this instability as a function of the experimental parameter space.

II. EXPERIMENTAL MOTIVATION

To motivate the theoretical investigation of this system, we shall describe a set of experiments (see PSBS for the experimental setup and independent measurements of the kinetic and material parameters) which clearly indicate the nature of the instability. (See Ref. 10 for other examples of chemical patterns driven by hydrodynamic instabilities.) The chemical reaction itself, sometimes called the blue bottle reaction, is well-documented.[11–13] As mentioned above, it consists of the alkaline oxidation of glucose by oxygen with methylene blue as a catalyst. The mixture is prepared and thoroughly mixed, thermostated for half an hour, further shaken and poured into an appropriate container (such as a Petri dish). Oxygen is allowed to diffuse into the system at the free surface from the atmosphere. After mixing, the system is saturated with O_2 and initially appears uniformly blue. After a period of time the mixture becomes colorless as the

---

[a)] Electronic mail: m.bees@surrey.ac.uk

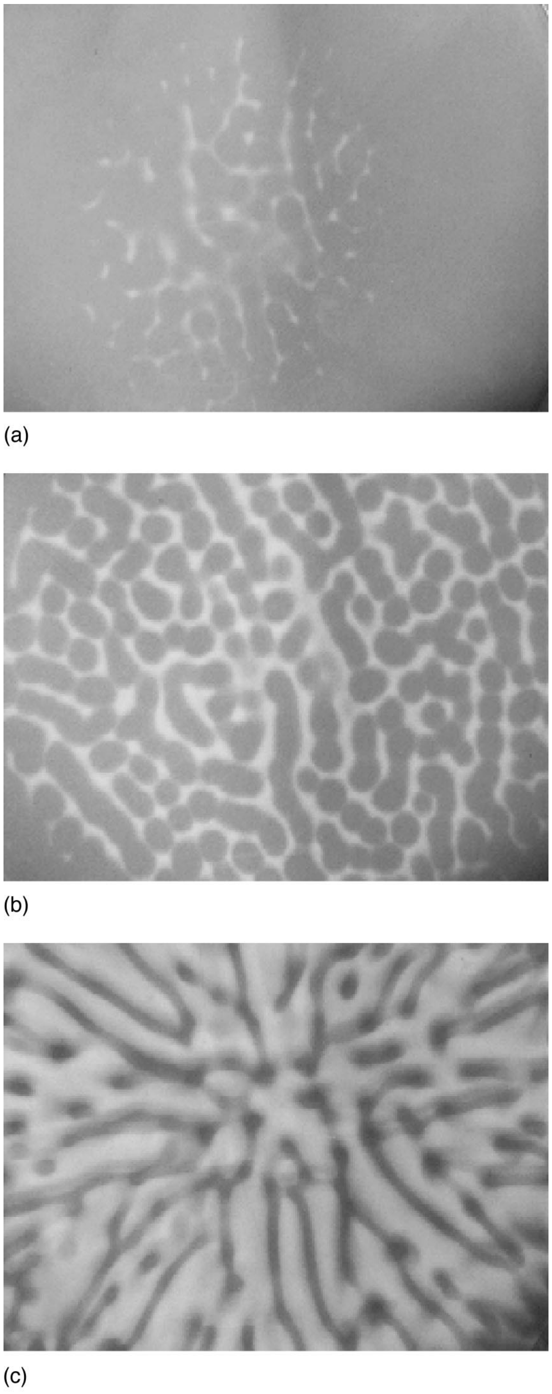

FIG. 1. Typical images of experiments conducted in a Petri dish with a free surface when increasing depth. Here, the horizontal size of the picture is 13.5 cm. Initial mixture: $[\mathrm{OH}^-]=0.020$ M, $[\mathrm{MB}^+]=4.6\times10^{-5}$ M, $[\mathrm{GL}]=0.054$ M. (Top) depth ≈ 5 mm; 5000 s after mixing. (Middle) depth ≈ 5 mm; 7000 after mixing. (Bottom) depth ≈ 15.5 mm; 4500 s after mixing.

oxygen is used up (except near the oxygen source) and thereafter a hydrodynamic instability arises and convection-like rolls or dots are formed.[14] In Fig. 1 we present images of the typical patterns produced when the depth of the mixture is varied. It is clear that although the patterns vary considerably in form, the wavelengths vary only by a factor of two. There are distinct similarities between these patterns, and the manner in which they arise, and those from bioconvection experiments,[15] which hints at the possibility of a similar mechanism for the instabilities.

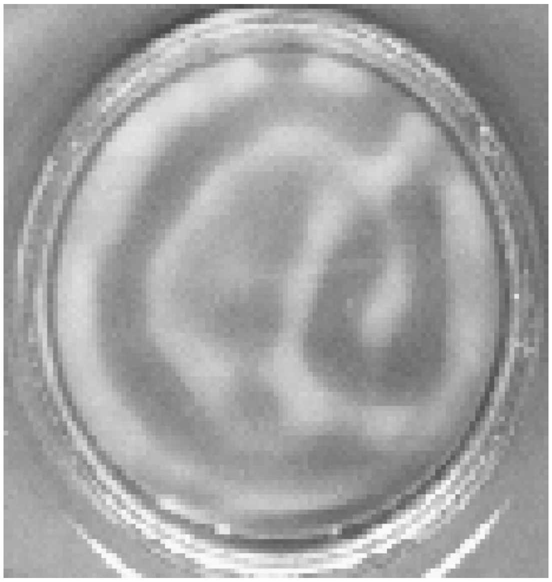

FIG. 2. An experiment conducted within a solid container with an oxygen permeable lid. The diameter of the petri dish is 5.1 cm and the picture was recorded approximately 5000 s after starting the experiment.

There are several possible explanations of this phenomenon. For instance, the free surface suggests that Marangoni effects might be involved. Clearly, evaporation can be significantly reduced by covering the Petri dish (which does not alter the observed patterns) although one may still not entirely rule out surface tension effects. However, when one removes the free surface altogether by enclosing the mixture in a solid container with an oxygen-permeable lid, an instability still arises, as is shown in Fig. 2. Of course, the presence of a solid upper boundary also changes the upper boundary condition from stress-free to no-slip and, consequently, one would expect the generated patterns to differ slightly, which is indeed observed. Furthermore, a solid container completely filled with the mixture but with a small hole drilled in the top produces a thin blue plume which gradually sinks to the bottom (see Fig. 3). This is clear evidence for an increase in reactant density due to oxidation. There may be other factors affecting the pattern formation when there is a free surface, but we believe that the increase in solution density at the upper surface due to the oxidation process is the most important driving mechanism for the instability.

III. MODEL EQUATIONS

The reactions can be summarized as follows (see PSBS; more details can be found in Adamčíková, Pavíková, and Ševčík):[16]

$$2\mathrm{MBH}+\mathrm{O}_2\rightarrow 2\mathrm{MB}^+ + 2\mathrm{OH}^-, \tag{1}$$

$$\mathrm{GL}+\mathrm{MB}^+ + \mathrm{OH}^-\rightarrow \mathrm{MBH}+\mathrm{GLA}, \tag{2}$$

where MB^+ is the blue oxidized form of methylene blue, MBH is the colorless reduced form, GL is glucose, GLA is

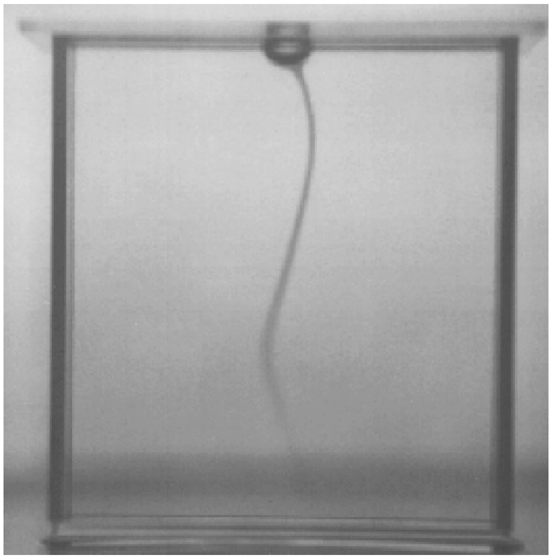

FIG. 3. An image of a plume descending from the area surrounding a small hole in the lid of an otherwise oxygen impermeable solid container. The width, height, and thickness of the container are 6.3 cm, 6.7 cm, and 1.3 cm, respectively.

gluconic acid, and the rate of Eq. (1) is much larger than that of Eq. (2). The concentration of glucose does not change significantly over a long period of time (one day) and so we assume that its concentration is kept constant, G_0, for a couple of hours during the experiments. The same argument applies for the concentration of OH^-.

We make the Boussinesq approximation that the change in density of the fluid adds only a vertical buoyancy term to the Navier–Stokes equations, and thus fluid flow is modeled as

$$\rho(\partial_t \mathbf{u} + (\mathbf{u}\cdot\nabla)\mathbf{u}) = -\nabla p - g\Delta\rho A\mathbf{k} + \mu\nabla^2\mathbf{u}, \tag{3}$$

and

$$\nabla\cdot\mathbf{u}=\mathbf{0}, \tag{4}$$

where $\mathbf{u}$ is the fluid velocity, A is the concentration of GLA (in terms of molarity, M), p is the pressure, ρ is the solution density, $\mathbf{k}$ is the unit vertical vector, and μ is the solution viscosity (see Table I). The constant $\Delta\rho$ is the molar excess solution density of GLA, with respect to GL, in terms of the units g/cm^3 M (as measured by PSBS). It is defined as $\rho_{\mathrm{GLA}}-\rho_{\mathrm{GL}}$, where ρ_{GLA} and ρ_{GL} are the densities of solutions of 1 M of GLA and GL, respectively. In the following, the spatial variations are restricted to two dimensions and we put $\mathbf{u}=(u,0,w)$. In accordance with experimental conditions we assume that the upper boundary is stress-free and the lower boundary has no-slip boundary conditions. Therefore,

$$w=w_{zz}=0 \quad \text{at} \quad z=0, \tag{5}$$

and

$$w=w_z=0 \quad \text{at} \quad z=-H. \tag{6}$$

Advective conservation and local production of reactants indicates that their concentrations, C (say), must obey an equation of the form

$$\partial_t C = -\nabla\cdot(C\mathbf{u}-D_C\nabla C)+I_C, \tag{7}$$

where D_C is the diffusivity of C and I_C indicates the rate of change of C due to the reactions. The large molecules have roughly the same rates of diffusion although the diffusivity of GLA varies slightly from that of MBH and MB^+. For the remainder of this article, we assume that the small oxygen molecule has a diffusivity of D_Ω, GLA has a diffusivity of D_A, and MBH and MB^+ each have a diffusivity of D. D is estimated to be approximately 4×10^{-6} cm^2/s using the fact that molecules in water with the same molecular weight have similar diffusion coefficients. The molecular weight of methylene blue, which is 319.86, is compared with that of saccharose with a molecular weight of 342 and a known diffusion constant of 4.2×10^{-6} cm^2/s in water at 25 °C. For the four chemical species $W=[\mathrm{MBH}]$, $B=[\mathrm{MB}^+]$, $A=[\mathrm{GLA}]$, and $\Omega=[O_2]$ we thus get that

$$\partial_t A = -\nabla\cdot(A\mathbf{u}-D_A\nabla A)+k_{\mathrm{obs}}B, \tag{8}$$

TABLE I. Parameter estimates (indicated by a *) and measurements (with appropriate s.f.).

Name	Description	Value or range	Units
H	suspension depth*	0–10	cm
D	diffusivity* of MBH and MB^+	4×10^{-6}	cm^2/s
D_A	diffusivity of GLA	6.7×10^{-6}	cm^2/s
D_Ω	diffusivity of oxygen	2.11×10^{-5}	cm^2/s
ρ	fluid density (∼water at 25 °C)	0.9970	g/cm^3
ρ_{GL}	solution density per M of GL	1.065 ± 0.009	g/cm^3
ρ_{GLA}	solution density per M of GLA	1.108 ± 0.009	g/cm^3
$\Delta\rho$	excess solution density per M of GLA (replacing M of GL)$=\rho_{\mathrm{GLA}}-\rho_{\mathrm{GL}}$	0.044 ± 0.018	g/cm^3 M
μ	dynamic viscosity* (∼water)	10^{-2}	g/cm s
ν	kinematic viscosity*	10^{-2}	cm^2/s
g	acceleration due to gravity	10^3	cm/s^2
k_1	fast reaction rate	2000	/Ms
k_{obs}	slow reaction rate	0.0042	/s
W_0	initial (homogeneous) concentration of MBH+MB^+	4.6×10^{-5}	M
Ω_0	concentration of O_2 at the free surface	2.6×10^{-4}	M
$\overline{H}$	sublayer depth $=\sqrt{D/k_{\mathrm{obs}}}$	0.031	cm

$$\partial_t B = -\nabla \cdot (B\mathbf{u} - D\nabla B) + 2k_1 \Omega W - k_{\mathrm{obs}} B, \tag{9}$$

$$\partial_t W = -\nabla \cdot (W\mathbf{u} - D\nabla W) - 2k_1 \Omega W + k_{\mathrm{obs}} B, \tag{10}$$

and

$$\partial_t \Omega = -\nabla \cdot (\Omega\mathbf{u} - D_\Omega \nabla \Omega) - k_1 \Omega W, \tag{11}$$

where k_{obs} is the effective rate constant of reaction (2) (PSBS). Adding Eqs. (9) and (10) we find that if the added concentration $B+W$ is homogeneous (equal to W_0, say) throughout the fluid at time zero then it will remain so. This allows us to make the simplifying assumption that

$$B + W = W_0. \tag{12}$$

Thus

$$\partial_t A = -\nabla \cdot (A\mathbf{u} - D_A \nabla A) + k_{\mathrm{obs}} B, \tag{13}$$

$$\partial_t B = -\nabla \cdot (B\mathbf{u} - D\nabla B) + 2k_1 \Omega (W_0 - B) - k_{\mathrm{obs}} B, \tag{14}$$

and

$$\partial_t \Omega = -\nabla \cdot (\Omega\mathbf{u} - D_\Omega \nabla \Omega) - k_1 \Omega (W_0 - B). \tag{15}$$

We must also have a source of oxygen at the upper boundary and no-flux boundary conditions such that

$$B_z = A_z = 0 \quad \text{and} \quad \Omega = \Omega_0 \quad \text{at} \quad z = 0, \tag{16}$$

and

$$B_z = A_z = \Omega_z = 0 \quad \text{at} \quad z = -H. \tag{17}$$

Nondimensionalizing B and A with W_0, Ω with Ω_0, length with the sublayer depth associated with reaction (2), $\overline{H} = \sqrt{D/k_{\mathrm{obs}}}$, and time with $1/k_{\mathrm{obs}}$ we get from Eqs. (13)–(15)

$$\partial_t A = -\nabla \cdot (A\mathbf{u} - \delta_A \nabla A) + B, \tag{18}$$

$$\partial_t B = -\nabla \cdot (B\mathbf{u} - \nabla B) + \kappa \Omega (1 - B) - B, \tag{19}$$

$$\partial_t \Omega = -\nabla \cdot (\Omega\mathbf{u} - \delta \nabla \Omega) - \lambda \Omega (1 - B), \tag{20}$$

and from Eq. (3)

$$S_c^{-1} [\partial_t \mathbf{u} + (\mathbf{u} \cdot \nabla)\mathbf{u}] = -\nabla P - RA\mathbf{k} + \nabla^2 \mathbf{u}. \tag{21}$$

$\overline{H}$ is a measure of the sublayer depth of reactions penetrating from the upper surface and gives the scaled fluid depth, d, as

$$d = \frac{H}{\overline{H}}. \tag{22}$$

Here, the two dimensionless reaction ratios κ and λ are given, respectively, by

$$\kappa = \frac{2k_1 \Omega_0}{k_{\mathrm{obs}}} \tag{23}$$

and

$$\lambda = \frac{k_1 W_0}{k_{\mathrm{obs}}}. \tag{24}$$

The two ratios of diffusivity δ and δ_A are defined, respectively, by

$$\delta = \frac{D_\Omega}{D} \tag{25}$$

TABLE II. Nondimensional parameters and their definitions.

Name	Description	Expression	Value or range
d	scaled fluid depth	$\frac{H}{\overline{H}}$	1 cm corresponds to 25.0
κ	reaction ratio	$\frac{2k_1\Omega_0}{k_{\mathrm{obs}}}$	248
λ	reaction ratio	$\frac{k_1 W_0}{k_{\mathrm{obs}}}$	21.9
δ	diffusion ratio	$\frac{D_\Omega}{D}$	5.28
δ_A	diffusion ratio	$\frac{D_A}{D}$	1.68
R	Rayleigh number	$\frac{g\Delta\rho W_0 \overline{H}^3}{\mu D}$	$50\,600\overline{H}^3 = 1.5$
S_c	Schmidt number	$\frac{\nu}{D}$	2500

and

$$\delta_A = \frac{D_A}{D}. \tag{26}$$

Also, the pair of dimensionless hydrodynamical parameters are the Rayleigh number given by

$$R = \frac{g\Delta\rho W_0 \overline{H}^3}{\mu D}, \tag{27}$$

and the Schmidt number expressed as

$$S_c = \frac{\nu}{D}, \tag{28}$$

in terms of the dynamic viscosity $\nu = \mu/\rho$ (see summary in Table II). The boundary conditions become

$$B_z = A_z = 0 \quad \text{and} \quad \Omega = 1 \quad \text{at} \quad z = 0, \tag{29}$$

and

$$B_z = A_z = \Omega_z = 0 \quad \text{at} \quad z = -d. \tag{30}$$

We note that there are other choices of nondimensionalization, but this choice enables us to investigate and compare the behavior of the main region of oxidation (sublayer depth) while varying the parameters. The kinetics for GLA imply that the average of A is monotonically increasing and never reaches a steady state. Taking account of this temporal variation in A, we approach the linear analysis by substituting the expression

$$A(x,z,t) = \langle A \rangle (t) + a(x,z,t) \tag{31}$$

into Eq. (18), where $\langle A \rangle$ indicates a space average of A and thus, by definition, $\langle a \rangle = 0$. Hence,

$$\partial_t \langle A \rangle = \langle B \rangle \tag{32}$$

and

$$\partial_t a = -\nabla \cdot (a\mathbf{u}) + \delta_A \nabla^2 a + B - \langle B \rangle. \tag{33}$$

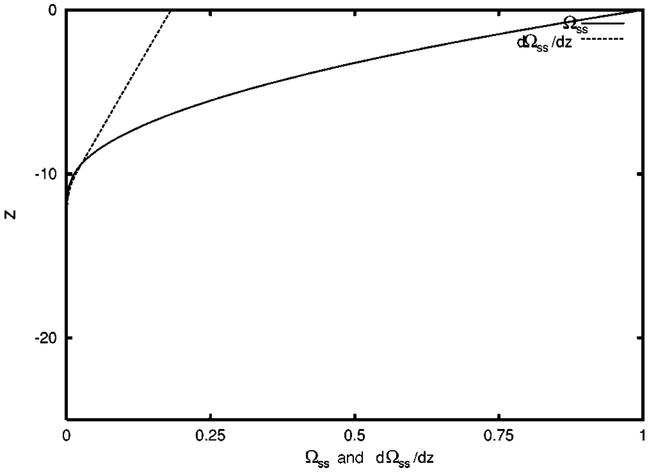

FIG. 4. Steady-state profile of oxygen concentration, $\Omega_{\rm ss}$, with depth, z, and its derivative for the reference parameter values ($d=25$, $\kappa=248$, $\lambda=21.9$, $\delta=5.275$, $\delta_A=1.675$ and $S_c=2500$).

IV. LINEAR ANALYSIS

From the governing equations we can find numerically a steady state solution $[a_{\rm ss}(z),B_{\rm ss}(z),\Omega_{\rm ss}(z)]$ with no flow ($\mathbf{u}=\mathbf{0}$), by solving the set of equations

$$
\begin{aligned}
d_z^2 a_{\rm ss} &= \frac{1}{\delta_A}(\langle B_{\rm ss}\rangle - B_{\rm ss}),\\
d_z^2 B_{\rm ss} &= B_{\rm ss} - \kappa\Omega_{\rm ss}(1-B_{\rm ss}),\\
d_z^2 \Omega_{\rm ss} &= \frac{\lambda}{\delta}\Omega_{\rm ss}(1-B_{\rm ss}),
\end{aligned}
\tag{34}
$$

where $d_z \equiv d/dz$, subject to the boundary conditions

$$d_z B_{\rm ss}|_{z=0} = d_z a_{\rm ss}|_{z=0} = 0, \quad \Omega_{\rm ss}|_{z=0} = 1,$$

and

$$d_z B_{\rm ss}|_{z=-d} = d_z a_{\rm ss}|_{z=-d} = d_z \Omega_{\rm ss}|_{z=-d} = 0. \tag{35}$$

We present typical profiles in Figs. 4–6. (See the Appendix for the numerical method.) These figures are a consequence of the balance between the chemical reactions and diffusion. The decay of the oxygen concentration, $\Omega_{\rm ss}$, from the upper surface is essentially due to the production of gluconic acid (with MB^+ as catalyst). The oxygen is almost completely depleted towards the bottom of the container.

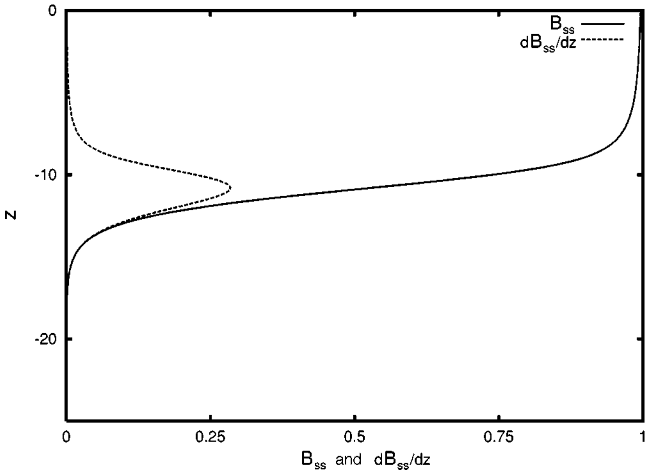

FIG. 5. Steady-state profile of the blue oxidized form of methylene blue concentration, $B_{\rm ss}$, with depth, z, and its derivative for the reference parameter values.

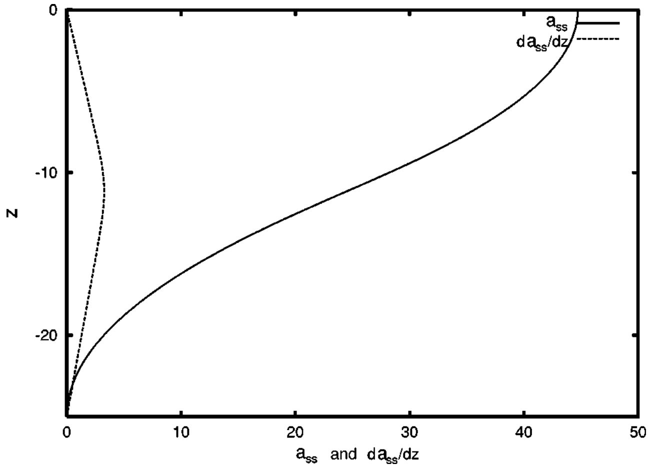

FIG. 6. Steady-state profile of $a_{\rm ss}$, the deviation of gluconic acid concentration from the mean, with depth, z, and its derivative for the reference parameter values. Note that $a_{\rm ss}$ is relevant up to the addition of an arbitrary constant as only the gradient is important to the dynamics. We set $a_{\rm ss}(z=-d)=0$ for convenience.

The colorless reduced form of methylene blue can be oxidized to form the blue variety. Hence, where the oxygen concentration is high, the concentration of MB^+ is also high (producing a plateau of saturated MB^+ at the upper surface). The production of gluconic acid, $a_{\rm ss}$, is directly related to the presence of MB^+. In particular, we expect that the deviation of the gluconic acid concentration with respect to its average will be greater when the variations in MB^+ are larger. The main driving force for the hydrodynamic instability is related to a gradient in solution density. We also note that the absolute concentration of $a_{\rm ss}$ does not appear in the linear analysis (see below) and only the gradient of $a_{\rm ss}$ is important. When this gradient is positive (see Fig. 6), we say that the stratification of the system is unstable and, if it is sufficiently large, will cause movement of the fluid.

We can establish the linear stability of these profiles in a similar style to analyses on convection and bioconvection.[1,17,18] We perturb the steady state solution such that

$$
\begin{aligned}
a &= a_{\rm ss}(z) + \epsilon a^1(x,z,t),\\
B &= B_{\rm ss}(z) + \epsilon B^1(x,z,t),\\
\Omega &= \Omega_{\rm ss}(z) + \epsilon \Omega^1(x,z,t),\\
P &= P_{\rm ss}(z,t) + \epsilon P^1(x,z,t),
\end{aligned}
\tag{36}
$$

and

$$\mathbf{u} = \epsilon \mathbf{u}^1(x,z,t).$$

Substituting these expressions and Eq. (31) into Eq. (21) and canceling quadratic and higher order terms in ϵ we obtain

$$S_c^{-1}\partial_t \mathbf{u}^1 = -\nabla P^1 - Ra^1\mathbf{k} + \nabla^2 \mathbf{u}^1, \tag{37}$$

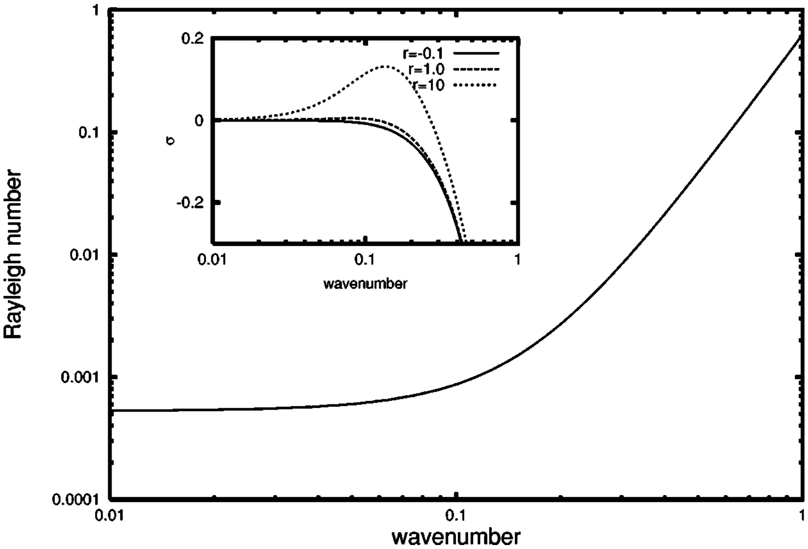

FIG. 7. The neutral stability curve for the reference parameter values (see Fig. 4). If the Rayleigh number takes a value above the lowest point of the neutral curve then a range of modes will become unstable. The growth rates of these modes vary with wavenumber as plotted in the inset for various values of the reduced Rayleigh number, $r=(R-R_c)/R_c$.

and similarly for the other equations. Calculating the divergence of Eq. (37) and the Laplacian of the third component of Eq. (37), respectively, yields

$$0=-\nabla^2 P^1 - R\partial_z a^1$$

and

$$Sc^{-1}\partial_t(\nabla^2 u_3^1) = -\partial_z \nabla^2 P^1 - R\nabla^2 a^1 + \nabla^4 u_3^1,$$

which are easily solved to obtain

$$Sc^{-1}\partial_t(\nabla^2 u_3^1) = R\partial_z^2 a^1 - R\nabla^2 a^1 + \nabla^4 u_3^1. \tag{38}$$

Introducing the normal modes

$$a^1 = \alpha(z)e^{ilx+\sigma t},$$

$$B^1 = \beta(z)e^{ilx+\sigma t},$$

$$\Omega^1 = \gamma(z)e^{ilx+\sigma t},$$

and

$$u_3^1 = U(z)e^{ilx+\sigma t}, \tag{39}$$

gives

$$\begin{aligned}
&(S_c^{-1}\sigma + l^2 - d_z^2)(d_z^2 - l^2)U = Rl^2\alpha,\\
&(\sigma + \delta_A(l^2 - d_z^2))\alpha = \beta - Ud_z a_{ss},\\
&(\sigma + (l^2 - d_z^2))\beta = \kappa\gamma(1-B_{ss}) - \kappa\beta\Omega_{ss} - \beta - Ud_z B_{ss},\\
&(\sigma + \delta(l^2 - d_z^2))\gamma = -\lambda\gamma(1-B_{ss}) + \lambda\beta\Omega_{ss} - Ud_z\Omega_{ss}.
\end{aligned} \tag{40}$$

Treating R as an eigenvalue to be found given the wave number l, we can compute the neutral curves (i.e.m such that $\sigma=0$), an example of which is displayed in Fig. 7 (see the Appendix for the numerical method). The figure indicates that the first mode to become unstable, as the Rayleigh number is increased above its critical value at R_c, has a wavenumber close to zero, corresponding to a very large wavelength. (An instability with a wavenumber of zero is never seen as this mode would also have a zero growth rate.) Therefore, in experiments with the Rayleigh number set infinitesimally greater than R_c, one should see a very large mode inhabiting the whole container. However, for a Rayleigh number that is significantly above the neutral curve other modes may grow faster. To illustrate this point, in the

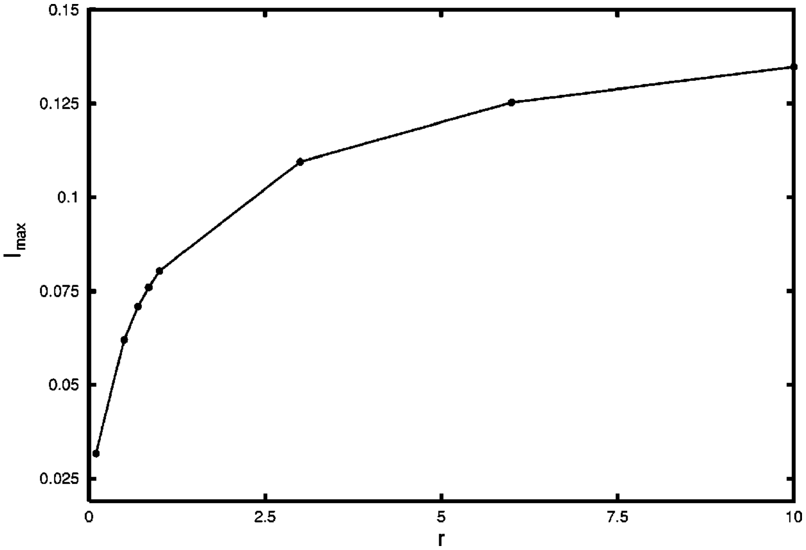

FIG. 8. The wavelength of the fastest mode, $l_{\max}$, for different values of the reduced Rayleigh number, for the reference parameter values.

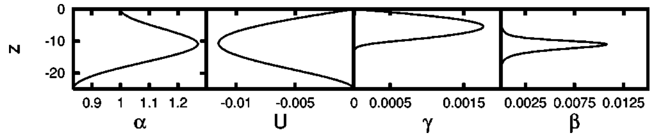

FIG. 9. The perturbation profiles of α, U, γ, and β, for the reference parameter values, and we set l equal to $l_{\max}$, the wavenumber with the greatest growth rate when $r=1$. Note: α refers to the GLA concentration perturbation, U is the z component of the fluid velocity perturbation, γ is the oxygen concentration perturbation, and β is the MB$^+$ concentration perturbation. For convenience we have arbitrarily set $\alpha(z=0)=1$ as this does not affect the linear analysis.

inset of Fig. 7 we plot the growth rates, σ, for some fixed values of the reduced Rayleigh number, $r=(R-R_c)/R_c$, close to R_c. From these graphs it is possible to read off the wavenumber of the fastest unstable mode. In Fig. 8 we plot the wavenumber of these most unstable modes as a function of r. This graph suggests that the most unstable wavenumber may tend to a limit as the Rayleigh number is increased, and further computations also indicate that the wavenumber is fairly insensitive to the value of r for large values. Taking $l_{\max}=0.13$, appropriate when $r=10$, corresponds to a wavelength of $2\pi/0.13\times\bar{H}\approx 48\bar{H}\equiv 48\sqrt{D/k_{\mathrm{obs}}}$. Clearly, this value also changes with the other key parameters. Hence, if $\bar{H}=0.031$ cm, a wavelength of $48\bar{H}\approx 1.5$ cm is predicted, which is in good agreement with the experimentally observed wavelengths under normal conditions of between 0.8 and 1.5 cm.

The increase in the value of the most unstable wavenumber as r is increased is a consequence of the expanding range of unstable modes. For unstable modes in general, the greater the wavenumber the quicker the mode grows until viscous and diffusive terms stabilize the dynamics for large values of l. In particular, the growth rate decreases to zero as $l\rightarrow 0$ as the time scale for the instability to occur on a large length scale must also be very large. The inset of Fig. 7 implies that the initially observed patterns for a reduced Rayleigh number of 10 should grow exponentially at a rate of $0.13\times k_{\mathrm{obs}}$ s^{-1} ≈ 2 h^{-1}, if the system had assumed the profile given by the steady state distribution.

It is clear from the neutral stability curve in Fig. 7 that the critical value of the Rayleigh number increases monotonically with the wavenumber. As the wavenumber becomes large it has the effect of increasing the magnitude of the viscous term in the first Eq. of (40). This must be balanced by the term on the right-hand side and, hence, $R_c \sim Ul^2/\alpha$. However, the second equation of the set implies that $l^2\alpha\sim U$ (assuming that the gradient of GLA is relevant to the instability and of order 1). Therefore, $R_c\sim l^4$ as $l\rightarrow\infty$. That is to say that the viscous terms in the horizontal directions stabilize the system. On the other hand, one may argue that there is no such mechanism available to stabilize the system for small values of l. We note that any balance between the terms of Eqs. (40) as $l\rightarrow 0$ must include the highest order derivative at leading order so that the nontrivial solutions satisfy the boundary conditions. Equally importantly we must ensure that the buoyancy term and driving gradient in GLA also appear at leading order so as to provide the basis for an unstable mode. Hence, the term in σ must be of a lower or equal order than the term in the highest derivative. The first of Eqs. (40) indicates, therefore, that

$$O(\sigma d_z^2 U)\leqslant O(d_z^4 U)=O(Rl^2\alpha).$$

Furthermore, variations with respect to z in U must be of the same order in l as U due to the boundary conditions and the fact that we are studying a mode-one solution. (However, variations with respect to z in α are not necessarily of the same order as α.) Hence,

$$U\sim Rl^2\alpha \quad \text{and} \quad \sigma\leqslant O(1).$$

The second of Eqs. (40) indicates that

$$O(\sigma\alpha)\leqslant O(d_z^2\alpha)=O(U),$$

and, hence, $d_z^2\alpha\sim Rl^2\alpha$ and

$$\sigma\leqslant O(Rl^2).$$

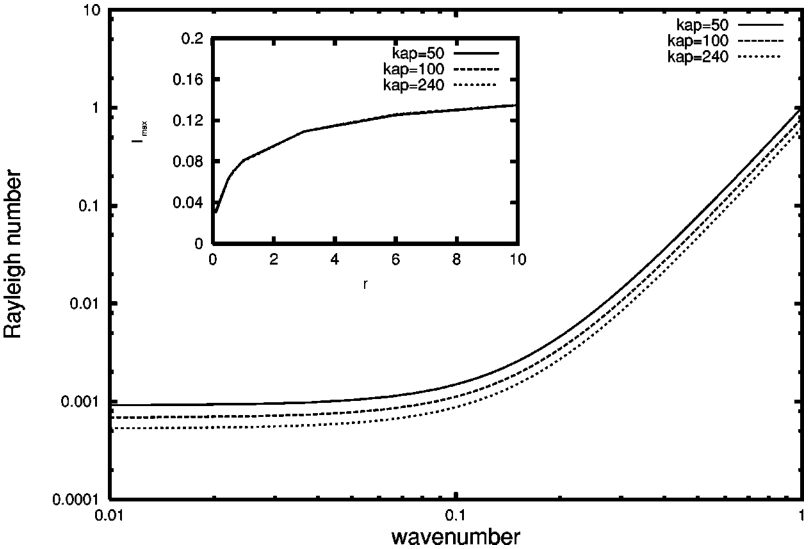

FIG. 10. The neutral stability curve for three values of κ, where $\lambda=21.9$, $\delta=5.275$, $\delta_A=1.675$, and $d=25$. The inset displays the wavelength of the fastest mode for these values of κ.

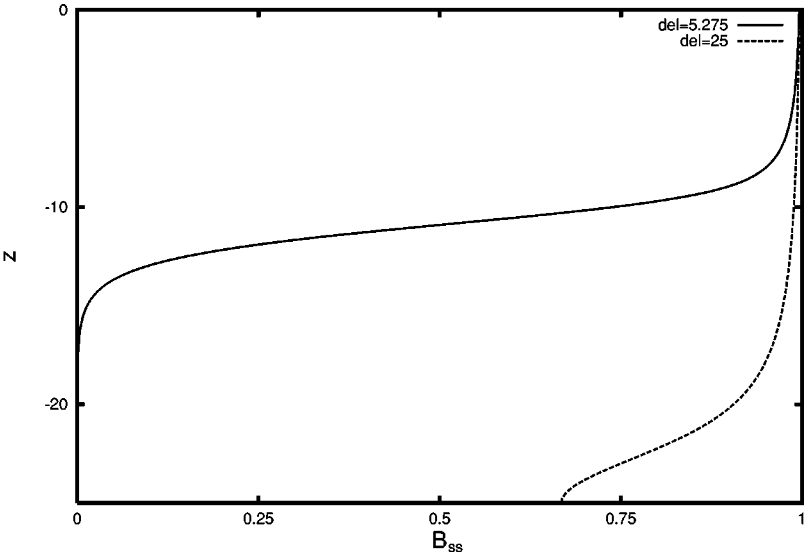

FIG. 11. The steady-state profiles of MB^+, B_{ss}, with varying δ, where $\lambda = 21.9$, $\kappa = 248$, $\delta_A = 1.675$, and $d = 25$.

This argument provides an upper bound on the value of σ as $l \to 0$ and implies that $\sigma \to 0$ (σ adopts this upper bound; see Fig. 7). The invariance of the perturbation equations under a constant translation in a_{ss} alone similarly leads to $\sigma = 0$ when $l = 0$. This is the analogue of the Saffman–Taylor invariance under translations when $l = 0$ and thus the system provides a good example of an instability of type II (Cross and Hohenberg).[19]

Some typical perturbation profiles are plotted in Fig. 9 for $l = l_{\max}$, the mode with the maximum growth rate, where $r = 1$. These profiles are as one would expect while taking account of the asymmetric boundary conditions and buoyancy term.

In what follows, we systematically explore the parameter space. To do this we change each parameter separately from the above parameter values, which we call the ''reference case,'' and analyze the resulting neutral stability curves.

Increasing κ has the same effect as either reducing the rate of reaction (2), increasing the rate of reaction (1), or increasing the partial pressure of oxygen at the liquid–gas interface. The profiles (not shown) of the steady states vary in the following way: The oxygen penetrates further in to the fluid from above, MB^+ follows suit, and the profile of GLA has larger gradients. In Fig. 10 we plot the neutral stability curves for a few values of κ. It is clear that the neutral curves are not very sensitive to variations in κ, although we remark that an increase in κ destabilizes the system. Also, from the plots of $l_{\max}$ with r, the most unstable wavenumber varies even less. This is due to the fact that the variable used in these plots is the reduced Raleigh number $[r = (R - R_c)/R_c]$ and the neutral stability curves can be superimposed by a translation in R. Increasing λ has a similar effect.

By increasing δ (similar results are also obtained by varying δ_A) one either increases the diffusivity of oxygen, D_Ω, or decreases the diffusivity of the larger molecules, D. The main effect is to increase the penetration of oxygen and thus to increase the plateau of MB^+. However, increasing δ too much can easily lead to a steady state profile in which the oxygen does not become significantly depleted in any part of the fluid and thus the concentration of MB^+ may not dip much below its saturated value, and the gradients in GLA can decrease (see Fig. 11). In this case, even if an instability

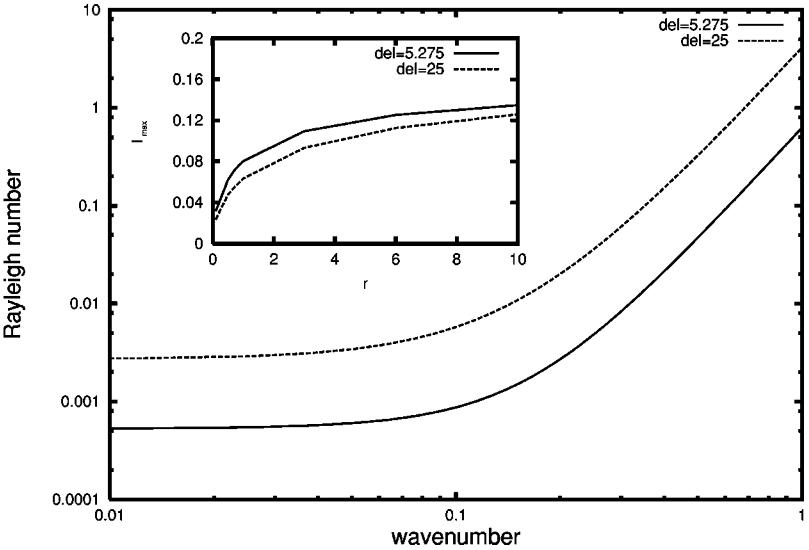

FIG. 12. The neutral stability curve for two values of δ, where $\lambda = 21.9$, $\kappa = 248$, $\delta_A = 1.675$, and $d = 25$. The inset displays the wavelength of the fastest mode for these values of δ. Similar results are obtained by varying δ_A.

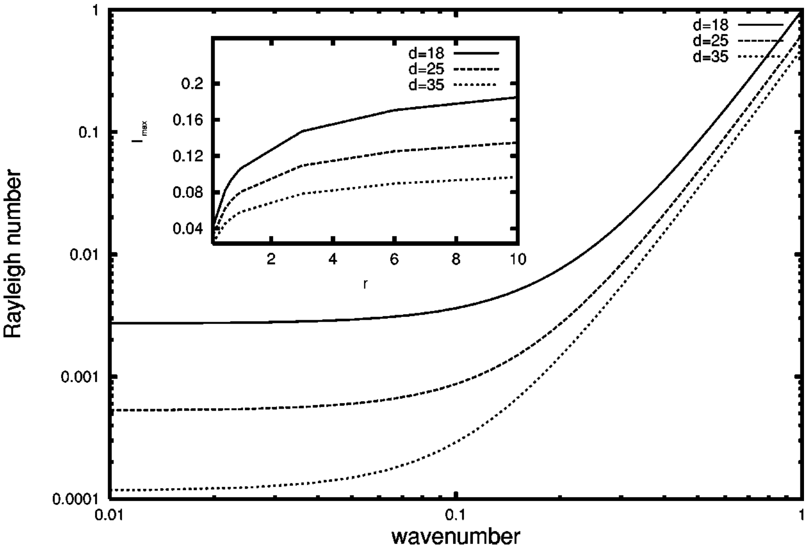

FIG. 13. The neutral stability curve for three values of d, where $\lambda = 21.9$, $\kappa = 248$, $\delta = 5.275$, and $\delta_A = 1.675$. The inset displays the wavelength of the fastest mode for these values of d.

arose because of significant GLA gradients, it may not be possible to observe the instability experimentally due the lack of contrast. The neutral stability curves while varying δ are displayed in Fig. 12. An increase in δ stabilizes the system and is associated with a small decrease in the most unstable wavenumber, as displayed in the inset.

A variation in the parameter d can be interpreted as a variation in the depth of the fluid relative to the sublayer depth (i.e., the penetration depth in which most of the chemistry takes place). Since d is not a chemical reaction parameter, it does not change the profiles of Ω_{ss} or B_{ss} significantly (for high enough d). However, the profile of a_{ss} does change as it is the deviation of $A(x,z,t)$ from its spatial average $\langle A\rangle(t)$, and this does depend on depth. $\langle A\rangle(t)$ decreases when d increases and this results in higher gradients of a_{ss} and thus a more unstable stratification. In Fig. 13 we plot the neutral stability curves and also the most unstable wavelengths for a range of values of r. The system is more unstable for higher values of d and, hence, R_c decreases. Clearly the neutral curves vary in a different manner to those studied previously and are difficult to superimpose by a translation in R alone. There is also an associated larger variation in the most unstable wavenumber, as displayed in the inset. As d increases, the mode-one solution has a smaller effective wavenumber in the vertical direction which will tend to force smaller wavenumbers in the horizontal direction to become more unstable. In other words, gradients of GLA over larger vertical distances will preferentially drive circulation with a larger horizontal length scale.

Preliminary experimental results suggest the following trends. By increasing the viscosity of the solution, using a small quantity of polyethyleneoxide, we find that the experimentally observed characteristic wavenumber decreases. This is consistent with the above theory as we would expect the Rayleigh number to decrease when viscosity increases and so the modes with higher wavenumbers become stable. We have also monitored the variation in observed characteristic wavenumber with an increase in solution depth. Although the pattern type changes from dots to lines, one can observe that a plateau of wavenumbers corresponding to a

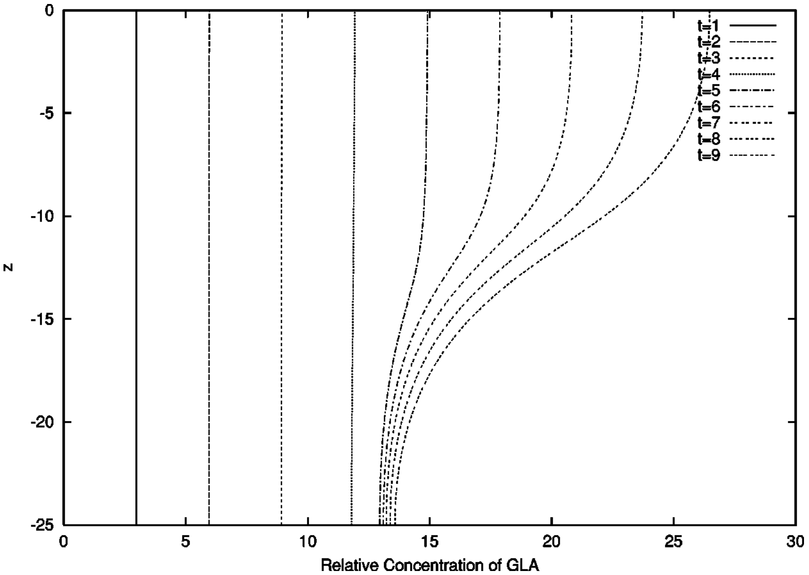

FIG. 14. The evolution of the horizontally uniform gluconic acid concentration profile with time, for the reference parameter values (see Fig. 4). Notice that we have allowed the mean of the concentration profile to increase with time here (the linear analysis is independent of this mean variation). Each time step represents a dimensional time of $3/k_{obs}$ s. When $k_{obs} = 0.0042$, this time step is 11.9 mins.

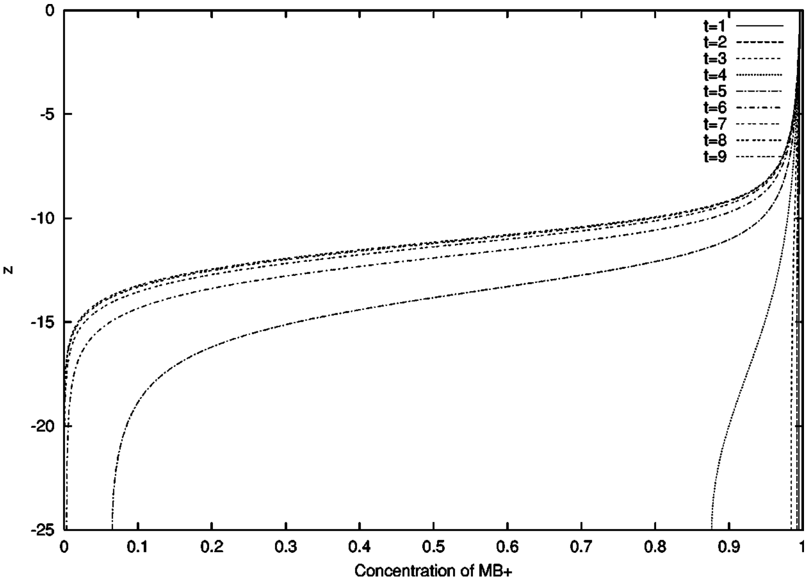

FIG. 15. The evolution of the horizontally uniform oxidized form of methylene blue concentration profile with time, for the reference parameter values. Equal time step as in Fig. 14.

wavelength of 0.8 cm for depths up to 8 mm is followed by a decrease in wavenumber down to a corresponding wavelength of 1.45 cm for a depth of approximately 12 mm. Again, these results are consistent with the neutral curves presented in Fig. 13 and their interpretation as discussed above. The full results of these and related experiments will be published in detail in a later report.

V. PSEUDOSTEADY-STATE LINEAR ANALYSIS

The above analysis explicitly assumes that the system does indeed reach the horizontally uniform steady-state profile, expressed by the solutions of Eqs. (34)–(35), immediately before a horizontally inhomogeneous mode grows. Starting from general initial conditions this is only possible after infinite time, although as the profiles approach the steady-state they vary very slowly with time. As the experimentally observed instabilities clearly arise in finite time, it is perhaps more appropriate to establish the effective linear stability of a pseudosteady-state profile. One might expect that the slowly varying profiles would become more unstable, with respect to horizontal variation, as they evolve towards the horizontally uniform steady-state profile and gradients in GLA increase. In other words, the effective neutral stability curve would be expected to decrease monotonically with time for any given horizontal wavelength. How this decrease occurs and the shape of the effective neutral curve for any given pseudosteady-state should be established. By continuity arguments, one might extrapolate general profile stability characteristics when the profiles are not varying so slowly.

From another more practical viewpoint, for any given Rayleigh number, the pseudosteady-state analysis will provide information concerning the time lapse required before an instability arises after the experiment is initiated from uniform initial conditions and thereafter the value of the linearly most unstable horizontal wavelength, which will vary with time.

Figures 14–16 indicate how the GLA, MB^+, and O_2

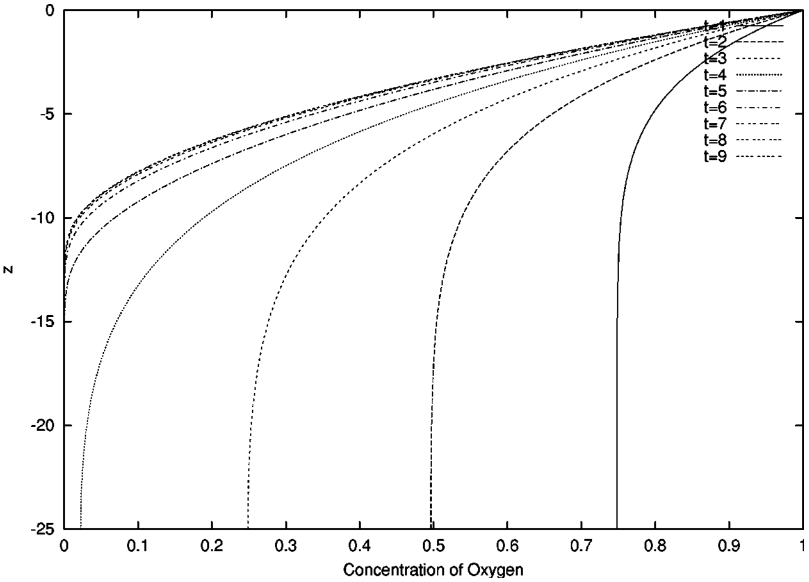

FIG. 16. The evolution of the horizontally uniform oxygen concentration profile with time, for the reference parameter values. Equal time step as in Fig. 14.

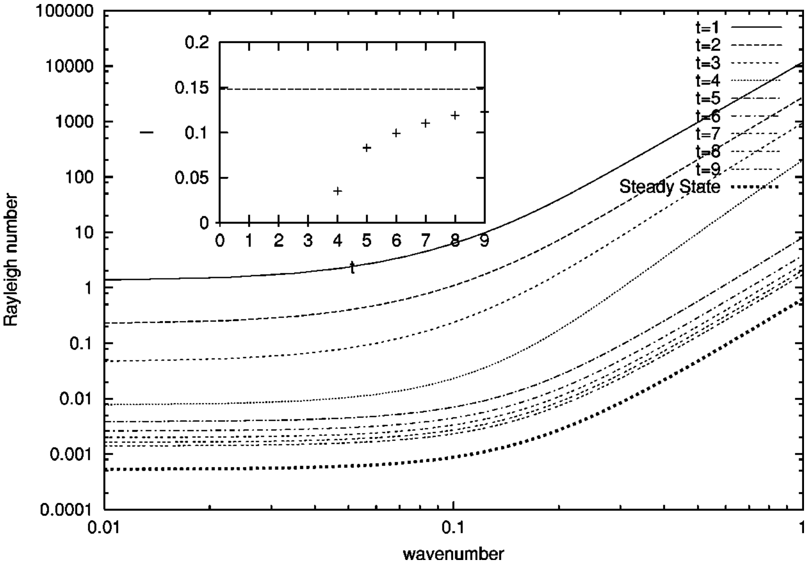

FIG. 17. The evolution of the neutral curve for the stability of the pseudosteady-state with time, for the reference parameter values. Equal time step as in Fig. 14. The final curve stands for the neutral stability curve for the horizontally uniform steady-state (here, the solution after 23 h; notice that it is identical to the neutral curve for the standard steady-state stability analysis). The inset indicates how the wavelength of the fastest growing mode from the horizontally uniform pseudosteady-state changes with time for a fixed Rayleigh number, $R = 0.01$. The straight line represents the wavenumber with the largest growth rate from the standard steady-state stability analysis.

concentration vary with time from uniform initial conditions (i.e., arbitrary GLA and saturated MB^+ and O_2 concentrations). We systematically recalculate the neutral curve from each of these profiles assuming each profile is varying only slowly with time and this variation can be neglected (Fig. 17). However, we note that when applying this assumption one should question the applicability of a couple of the neutral curves for which the concentration profiles are not changing so slowly. For a given Rayleigh number ($R = 0.01$) we plot in the inset of Fig. 17 the effective most unstable wavenumber as the profiles evolve from a uniform steady-state to illustrate the above comments.

VI. CONCLUSION

We have summarized a series of experiments, investigated in detail in PSBS, that provide good evidence for the existence of an overturning instability induced by chemical reactions. Furthermore, we have introduced a mathematical model, which adequately describes the phenomenon, and performed stability analyses on steady- and pseudosteady-states in order to predict the characteristic length and time scales of the initial instability. These predictions are in agreement with experimental results without the need for free parameters.

An extension to the above analyses would be to investigate the weakly nonlinear behavior of the instability close to the critical Rayleigh number and establish whether the bifurcation is subcritical or supercritical. In the case where the minimum of the neutral stability curve occurs at a wavenumber of zero, then long wavelength analysis is appropriate.[20,21] Furthermore one could extend the analysis to investigate the stability of a range of planforms and establish the preferred pattern.[22–24] It is possible that further instabilities will arise in the nonlinear regime due to the advection of reactants initiated by the linear instability.

Work is also in progress by the authors to systematically extend the above comparisons of theory with experiments and further characterize the instability mechanism.

ACKNOWLEDGMENTS

M.A.B. wishes to thank The Danish Research Academy for initial financial support and the European Community—Access to Research Infrastructure action of the Improving Human Potential Programme for support during collaborative visits. Part of this work was supported by the TMR-Network on Patterns, Noise, and Chaos, Project No. ERBFMRXCT960085. We also acknowledge support from DGES, Project PB96-1001 and Comissionat per a Universitats i Recerca (Generalitat de Catalunya), Project 1997SGR00090.

APPENDIX

The numerical method used in Sec. IV is a standard implementation of a fourth-order finite difference scheme, originally supplied by Dr. D. R. Moore (see Cash and Moore),[25] that uses the Newton–Raphson–Kantorovich algorithm. For the steady states, the program searches for solutions to Eqs. (34) which satisfy the boundary conditions, given initial guesses. The spatial average in the first of these equations is calculated at each iteration using a suitably accurate integration scheme. With regard to the perturbation equations, the program searches for the neutral stability curve (or growth rate if given a Rayleigh number) of Eqs. (40). For each wavenumber, initial guesses for the concentration, velocity field, and the Rayleigh number were provided, when necessary. Stretched meshes were employed to help resolve the boundary layer at the upper surface in deep layers and thus an accuracy of six significant figures was always achieved for convergence.

In Sec. V a set of partial differential equations (in one spatial and one temporal dimension) is solved. Newton's method is used to do this efficiently, employing band-diagonal LU decomposition[26] and a semi-implicit scheme. The equations are produced in the following manner: time derivatives are replaced by their forward differences and other terms are replaced by weighted averages of the future (unknown) values of the variables and their present (known) values. Initial guesses of the solution and the value of the time step can be controlled such that a minimal number of iterations is required for convergence. This method was highly successful and usually required two or less iterations for convergence at each time step.

[1] S. Chandrasekar, *Hydrodynamic and Hydromagnetic Stability* (Oxford University Press, London, 1961).
[2] S. Childress, M. Levandowsky, and E. A. Spiegel, J. Fluid Mech. **69**, 595 (1975).
[3] T. J. Pedley and J. O. Kessler, J. Fluid Mech. **212**, 155 (1990).
[4] R. V. Vincent and N. A. Hill, J. Fluid Mech. **327**, 343 (1996).
[5] A. J. Hillesdon, T. J. Pedley, and J. O. Kessler, Bull. Math. Biol. **57**, 299 (1995).
[6] T. J. Pedley and J. O. Kessler, Annu. Rev. Fluid Mech. **24**, 313 (1992).
[7] M. A. Bees, N. A. Hill, and T. J. Pedley, J. Math. Biol. **36**, 269 (1998).
[8] M. A. Bees and N. A. Hill, J. Math. Biol. **38**, 135 (1999).
[9] A. J. Pons, F. Sagués, M. A. Bees, and P. G. Sørensen, J. Phys. Chem. B **104**, 2251 (2000).
[10] D. Avnir and M. L. Kagan, Chaos **5**, 589 (1995).
[11] J. Campbell, J. Chem. Educ. **40**, 578 (1963).
[12] L. Adamčíková and P. Ševčík, J. Chem. Educ. **75**, 1580 (1998).
[13] W. Vandaveer and M. Mosher, J. Chem. Educ. **74**, 402 (1997).
[14] L. Adamčíková and P. Ševčík, Z. Naturforsch. A: Phys. Sci. **52a**, 650 (1997).
[15] M. A. Bees and N. A. Hill, J. Exp. Biol. **200**, 1515 (1997).
[16] L. Adamčíková, K. Pavíková, and P. Ševčík, Int. J. Chem. Kinet. **31**, 463 (1999).
[17] N. A. Hill, T. J. Pedley, and J. O. Kessler, J. Fluid Mech. **208**, 509 (1989).
[18] M. A. Bees and N. A. Hill, Phys. Fluids **10**, 1864 (1998).
[19] M. C. Cross and P. C. Hohenberg, Rev. Mod. Phys. **65**, 851 (1993).
[20] S. Childress and E. A. Spiegel (unpublished).
[21] C. J. Chapman and M. R. E. Proctor, J. Fluid Mech. **101**, 759 (1980).
[22] M. Golubitsky, J. W. Swift, and E. Knobloch, Physica D **10**, 249 (1984).
[23] E. Knobloch, Physica D **41**, 450 (1990).
[24] A. M. Metcalfe and T. J. Pedley, J. Fluid Mech. **370**, 249 (1998).
[25] J. R. Cash and D. R. Moore, BIT **20**, 44 (1980).
[26] W. H. Press, S. A. Teukolsky, W. T. Vetterling, and B. P. Flannery, *Numerical Recipes in FORTRAN. The Art of Scientific Computing*, 2nd ed. (Cambridge University Press, Cambridge, 1992).